


 Cite this: *RSC Adv.*, 2021, **11**, 27757

Exploring the feasibility of liquid fuel synthesis from CO_2 under cold plasma discharge: role of plasma discharge in binary metal oxide surface modification[†]

 Nitesh Joshi  and L. Sivachandiran*

The conversion of CO_2 to CH_3OH over binary mixed metal oxides of $\text{NiO}-\text{Fe}_2\text{O}_3$ is investigated in the study. A series of catalysts, *i.e.*, NiO , Fe_2O_3 , 5% $\text{NiO}-\text{Fe}_2\text{O}_3$ (5NF), 10% $\text{NiO}-\text{Fe}_2\text{O}_3$ (10NF), and 15% $\text{NiO}-\text{Fe}_2\text{O}_3$ (15NF), was tested for CO_2 conversion and CH_3OH selectivity performance. The results show that binary mixed metal oxides are more active in comparison to pure metal oxides. Moreover, increasing NiO mixing leads to the agglomeration of NiO particles. At 200 °C, around 1.5%, 2%, and 3.2% CO_2 conversion is achieved for 5NF, 10NF, and 15NF, respectively. Interestingly, when cold plasma was ignited at 200 °C, around 5.4%, 6.2%, and 10.2% CO_2 conversion was achieved for the 5NF, 10NF, and 15NF catalysts, respectively. 15NF exhibited the highest CO_2 conversion, but produced only CH_4 . Plasma coupling with the catalyst led to an increase in the CH_3OH yield, and around an 5.8-fold enhancement was achieved with 10NF at 200 °C compared to thermal catalysis. We showed that the combination of plasma and thermal heating brings about significant changes to the catalyst morphology, which significantly improved the catalytic activity. X-ray diffraction (XRD) and X-ray photoelectron spectroscopy (XPS) characterization revealed that plasma treatment leads to the formation of a mixture of spinel compounds ($\text{NiO}-\text{Fe}_2\text{O}_3$, NiFe_2O_4 , and Fe_3O_4).

 Received 22nd June 2021
 Accepted 19th July 2021

 DOI: 10.1039/d1ra04852j
rsc.li/rsc-advances

1. Introduction

The rising CO_2 concentration in the atmosphere is a serious situation. Currently, the adverse effects triggered by CO_2 emissions are being well documented and are causing global concern.^{1–3} There are various methodologies available for controlling rising CO_2 levels. Among the viable solutions, great efforts have been made in terms of two strategies: (1) CO_2 capture and storage^{4,5} (2) CO_2 chemical recycling.^{6,7} It has been reported that the recycling of CO_2 as a carbon source for value-added chemical production, such as methane (CH_4),⁸ methanol (CH_3OH)⁹ or polycarbonate,¹⁰ would be considered to be a more sustainable use of global carbon resources, which would lead to lower consumption of fossil fuels and subsequent CO_2 emissions.^{11,12} Among the different alternatives, one of the widely investigated processes is the hydrogenation of CO_2 to CH_3OH (eqn (1)) using H_2 produced from renewable energy sources.

CH_3OH is one of the most important feedstocks as it can be used directly as a fuel, as an energy carrier in fuel cells, or as a raw material to synthesis formaldehyde, acetic acid, and

olefins.¹¹ CH_3OH is traditionally produced from syngas, however, for economic and environmental reasons, there is great interest in developing a process where it is produced from the greenhouse gas CO_2 . The main problem that is currently hindering the wider application of the latter process is low CH_3OH selectivity due to the occurrence of the competitive reverse water–gas shift (RWGS) reaction (eqn (2)).¹³ Thus, it is important to develop catalytic materials characterized by high activity and selectivity towards CH_3OH .

The state-of-the-art catalyst for CH_3OH synthesis is $\text{CuO}/\text{ZnO}/\text{Al}_2\text{O}_3$ (CZA), where CuO and ZnO catalyse both the CH_3OH formation and the RWGS reaction.¹³ The reaction is catalysed at 513–533 K under 50–100 bar pressure.¹³ The commercial catalyst CZA losses its activity after several catalytic cycles due to surface poisoning and particle sintering. Additionally, to catalyse a reaction *via* thermal catalysis, a high operating temperature and pressure are applied to overcome kinetic and thermodynamic barriers.^{9,14} Thus, the industrialization of the CH_3OH production requires an efficient catalyst with a low activation temperature.

The impact of metal ions in bimetallic catalysts is crucial, as demonstrated by Ren *et al.*,¹⁵ where in their study $\text{Ni}-\text{M}/\text{ZrO}_2$ catalysts exhibited different product distributions with different metal ions. Iron (Fe)-based catalytic systems have been widely investigated, due to their low cost and high activity, for RWGS

Laboratory of Plasma Chemistry and Physics (LPCP), Department of Chemistry, Faculty of Engineering and Technology, SRM Institute of Science and Technology, SRM Nagar, Kattankulathur, Chennai-603203, India. E-mail: sivachal@srmist.edu.in

† Electronic supplementary information (ESI) available. See DOI: 10.1039/d1ra04852j



and Fischer Tropsch (FT) reactions to synthesis olefinic products.¹¹ Gasoline fractions have been reported to be produced by Wei *et al.*¹⁶ using a heterogeneous catalytic system of Na-Fe₃O₄/HZSM-5. Herein, a CO₂ hydrogenation reaction was initiated at a H₂/CO₂ ratio = 3, 320 °C, 2 MPa pressure and ~67 mL min⁻¹ feed flow rate. The authors obtained gasoline (C5 to C11 hydrocarbons with 78% selectivity) from this setup. In another study, Zhou *et al.*¹⁷ employed ZnO/ZrO₂ integrated over H-ZSM5 for aromatic synthesis from CO₂. The authors obtained 16% CO₂ conversion and 76% selectivity towards aromatics at 340 °C under 40 bar pressure. Additionally, there are some state-of-the-art reviews available that comprehensively summarize the recent advancements in heterogeneous catalysis for CO₂ hydrogenation to value added products.^{18,19}

There are few reports available on CO₂ reduction using mixed oxides under plasma discharge. CO₂ conversion to CH₄ has been carried out using NiO-Fe₂O₃ layered double hydroxides by Wierzbicki *et al.*²⁰ Around 75% CO₂ conversion and 100% CH₄ selectivity were obtained using a Ni₂₀Fe_{1.5} catalyst at 250 °C and 11.7 W input power. In another study, CO₂ conversion to syngas using a Ni/Al₂O₃ catalyst was carried out by Ma *et al.*²¹ using plasma. The authors applied 55.4 J cm⁻³ of specific input energy and around 14% CO₂ conversion was achieved, with CO being the main product quantified at the reactor outlet. Jwa *et al.*²² carried out CO and CO₂ conversion to CH₄ over a Ni-zeolite catalyst. The authors studied the influence of external heating on the activity of the catalysts. At a temperature of 180–360 °C, the CO₂ conversion was <15%. Upon combining thermal heating with plasma discharge on the catalyst bed, the CO₂ conversion increased to >95%. This enhancement is the result of the reactive species generated in the plasma reducing the catalyst activation energy barrier and thermal heating facilitating their interaction.

When it comes to the activation of catalysts and the conversion of reactants under ambient conditions, non-thermal plasma (NTP) aided catalysis is a fascinating avenue. NTP is efficient for activating CO₂ at room temperature under atmospheric pressure conditions.^{23,24} The NTP process of catalysis operates *via* a completely different mechanism of electron impact dissociation, thus, it consumes less energy compared to thermal catalysis. In thermal catalysis, the vibrational excitation of molecules is a key factor that requires higher energy and therefore impacts the overall energy efficiency.²⁵ Various types of NTPs have been employed in the successful conversion of CO₂ to CO or CH₄ or oxygenates.^{14,26–30} The dielectric barrier discharge (DBD) is one such NTP that has been widely studied, as it has a simplistic design and is operational under ambient conditions. Thus, it could be of prime importance from a commercialisation point of view. In terms of DBD plasma, only a handful of studies have focused on the conversion of CO₂ to oxygenate. For instance, Bill *et al.*³¹ showed around 0.2% CH₃OH yield by using 400 W input power at a 250 mL min⁻¹ feed flow rate. Interestingly, the commercial CH₃OH catalyst Cu/ZnO/Al₂O₃ under atmospheric pressure shows 12% CO₂ conversion and a CH₃OH selectivity of 0.4%, but upon increasing pressure to the 8 bar, the conversion rose to 14% with 10% CH₃OH selectivity.³² Enhanced CO₂ conversion to

CH₃OH was reported by Wang *et al.*²⁴ The authors showed that CH₃OH selectivity could be increased to 53.7% with 11% yield using Cu/γ-Al₂O₃ at room temperature under atmospheric pressure. More recently, a Co_xO_x/MgO catalyst system was employed for the conversion of CO₂ to CH₃OH at room temperature under atmospheric conditions.³³ The authors observed that 33% CO₂ conversion and 31% CH₃OH selectivity were achieved using 10 W of input power.

In our previous work, we successfully showed that binary mixed metal oxides are more active towards CO₂ conversion and CH₃OH production.³⁴ The main aim of this work was to employ mixed binary metal oxides of NiO-Fe₂O₃ for the hydrogenation of CO₂ to CH₃OH using non-thermal plasma. Dedicated efforts were made to investigate (i) the influence of individual and binary mixed metal oxides on CO₂ conversion and CH₃OH production, (ii) the impact of NiO mixing on Fe₂O₃ for CO₂ conversion and CH₃OH selectivity, (iii) understanding the role that plasma power and operating temperature have on CO₂ conversion and products distribution, and (iv) the effect that plasma discharge has on catalyst surface modification.



2. Experimental description

2.1. Preparation of the catalyst

In this study, the amount of NiO was varied: 5%, 10% and 15% on Fe₂O₃ and labelled as 5NF, 10NF and 15NF, respectively. The detailed NiO-Fe₂O₃ catalyst synthesis procedure has been reported elsewhere.³¹ Briefly, various amounts of Ni(NO₃)₂·6H₂O (99% pure) were mixed with Fe(NO₃)₃·9H₂O (99% pure) and dissolved in 50 mL of ethanol (96% pure) and a homogeneous solution was made with constant stirring. Then, the precursor was precipitated as hydroxide sol using 10% NH₄OH solution at a flow rate of 1 mL min⁻¹. At pH ~ 12, complete precipitation was reached, then the sol was aged at 85 °C overnight. Then the precipitate was centrifuged-washed several times using distilled water to remove the impurities. The washed residue was dried at 100 °C (for 2 h) and then calcined at 600 °C for 3 h.

2.2. Catalyst characterization

The synthesised and used catalysts were characterised by different techniques. X-ray diffraction (XRD) data were obtained using a PANalytical X'pert3 instrument [Cu K α 1.54 Å, 40 kV, 40 mA]. The catalyst surface morphology was studied using nanoscale images obtained using a high-resolution field emission electron microscopy (FESEM, Quanta 200) and high-resolution transmission electron microscopy (HRTEM JEOL, Japan) instruments. Along with electron images, energy-dispersive X-ray (EDX) spectroscopy data was obtained to determine the elemental composition, which is provided in Fig. S1a–c in the ESI.† The elemental mapping image of 10NF is provided in Fig. S1d in the ESI,† which was obtained using

FESEM. X-ray photoelectron spectroscopy (XPS) analysis was carried out using a PHI Versaprobe III to obtain further information on the elemental composition and oxidation state of the catalysts. The physical properties of the catalysts, *i.e.*, the total surface area (Brunauer–Emmett–Teller, BET) was measured using an Autosorb iQ Station at 77 K by N₂ physisorption. Before the analysis, the catalysts were degassed under a He atmosphere at 150 °C for 3 h. The data from the N₂ sorption study is provided in Fig. S2 in the ESI.† The Lewis and Brønsted acidic sites were determined using Fourier-transform infrared (FTIR) spectroscopy (SHIMADZU IR TRACER-100) by adsorbing pyridine. 10 mg of pyridine adsorbed catalysts were thoroughly mixed with 100 mg of NaCl to maintain sample uniformity and were then analysed by FTIR spectroscopy in attenuated total reflectance (ATR) mode. The FTIR analysis is reported in Fig. S3 in the ESI.†

2.3. Plasma reactor and experimental setup

The experimental setup employed in this study is shown in Fig. 1. A detailed description of the reactor has been reported elsewhere.³¹ Briefly, in this setup the cylindrical quartz tube is 600 mm in length, the outer diameter (OD) of the tube is 25 mm, the wall thickness of the tube is 3 mm and the inner diameter (ID) of the reactor is 19 mm. A 12 mm (OD) stainless steel rod is used as an inner electrode, which leads to a 3.5 mm discharge gap. In the experiments, the discharge length was fixed at 100 mm by wrapping the quartz tube in stainless steel mesh. The plasma was generated using a step-up transformer supplied by Jayanti Transformer (Chennai, India). The AC voltage was varied from 10 to 18 kV at a constant frequency of 50 Hz.

The electrical parameters were calculated using two high voltage probes with 1 : 100 attenuation (Zeal Manufacturing Service Limited, Pune, India), which were connected to an oscilloscope (Keysight, 70 MHz 2G a s⁻¹) as shown in Fig. 1. The power dissipated into the reactor was calculated using the Lisajous method.^{35,36}

For catalytic CO₂ conversion, the binary metal oxides (0.5 g) were placed in the centre of the quartz tube and quartz wool (QW 3.67 g) was used to sandwich the catalyst. The catalyst packing mode used in this work is different from that in our previously reported work.³¹ In the previous study, the catalyst was loaded on QW using a dip-coating method. However, in this study, due to practical issues related to catalyst

characterisation, before and after plasma treatment, the catalyst was packed in sandwich mode. The CO₂ and H₂ composition was set to a ratio of 1 : 3 and the total flow rate was fixed at 100 mL min⁻¹. The discharge volume was fixed to 17.4 cm³.

The feed flow rate through the reactor was fixed to 100 mL min⁻¹ unless otherwise mentioned, and H₂ and CO₂ were mixed in a 3 : 1 ratio. Commercial-grade CO₂ (99.5%), H₂ (99.99%), N₂ (99.999%) and zero air (99.999%) were supplied by Rana Industrial gases (Chennai, India). The zero air was used for catalyst pre-treatment and N₂ was used as a dilutant gas during gas chromatography (GC) calibration. The CO₂ and H₂ flow were regulated using the respective calibrated mass flow controllers (MFC, KOFLOC, Japan).

2.4. Methodology and product analysis

The gaseous products at the reactor outlet were analysed using gas chromatography (GC, Perkin Elmer-Claraus 580) equipped with an online gas sampling loop (2 mL). A thermal conductivity detector connected to a ShinCarbon ST Column (mesh size of 100/120, length of 2 m and an inner diameter of 1/11th inch) was used for eluting the reactants and products. The reaction output, such as CO₂ conversion, product selectivity and product yield, was calculated using the equations provided in the ESI.†

2.5. Experimental procedure

2.5.1. Thermal catalysis. As shown in Fig. 1, a K-type thermocouple placed inside the reactor, on QW, was used to monitor the catalyst temperature. For all of the experiments, a fresh catalyst was used, and before each experiment, the catalyst was pre-treated under zero air at 300 °C for 1 h. Then, the reactor was cooled to room temperature. At room temperature, the feed gas was sent to the reactor and the blank concentrations of CO₂ and H₂ were obtained after reaching the adsorption/desorption equilibrium. To understand the effect of temperature on the CO₂ conversion and CH₃OH selectivity, the catalyst bed temperature was varied between 100 and 250 °C. Online sampling was carried out after 60 min of reaching the set temperature (steady state). For each set temperature, a minimum of three samples were analysed to ensure reproducibility and each experiment was repeated a minimum of three times.

2.5.2. Plasma and thermal-plasma catalysis. For the thermal-plasma catalytic process, the plasma discharge was ignited after reaching the thermal catalytic steady state (about 30 min of the thermal catalytic process at the set temperature). The online sampling was performed after 10 min of continuous plasma treatment. It is noteworthy to mention that during plasma treatment the furnace was switched off to avoid electrical perturbation. However, the temperature difference before and after plasma treatment was around ±10 °C.

3. Results and discussion

3.1. Physicochemical characterization of the catalysts

The XRD patterns of the synthesised catalysts are shown in Fig. 2. The XRD patterns show that the synthesized catalysts are

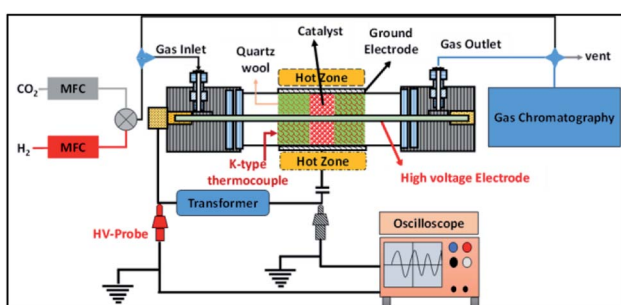


Fig. 1 A schematic diagram of the experimental setup.



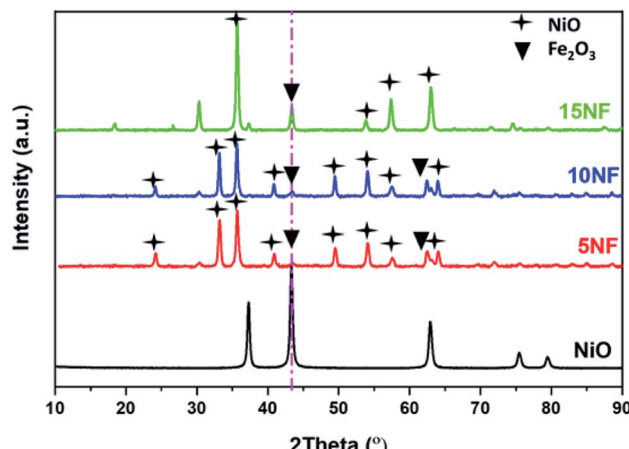


Fig. 2 XRD characterization of the synthesised catalysts.

pure and crystalline. The diffraction peaks at 37.3, 43.3, 62.9 and 75.3 confirm the presence of NiO, which correspond to the (111), (200), (220), and (311) planes, respectively. For NiO–Fe₂O₃ binary mixed oxides, the characteristic peak for NiO, centred at 43.3°, is used for calculating the particle size, whereas the intense peak at 33° is used to calculate the particle size of Fe₂O₃. The details of particle size calculations using the Scherrer equation for all of the catalysts are presented in Table 1. It can be observed that the particle size of NiO increases upon increasing the % of metal oxide mixing. This is due to the weak interaction between NiO and Fe₂O₃, which does not suppress the agglomeration and formation of large NiO clusters unlike on other supports, such as porous Al₂O₃, which interacts

strongly with active metals to suppress particle growth.^{37,38} However, as compared in Table 1, the Fe₂O₃ particle size was not significantly affected due to the dopant action of NiO.

Fig. 3 shows the FESEM images of the various catalysts. As can be seen from Fig. 3(a), on 5NF the NiO particles are uniformly distributed, on the other hand for 10NF and 15NF the NiO particles are aggregated upon increasing the amount of metal mixing, as can be seen from Fig. 3(b) and (c), respectively. It should be noted that the particle size calculated from the XRD data (using the Scherrer equation) is in good agreement with what is observed in the SEM images. It can be observed that, on the one hand, the increase in NiO mixing leads to an increase in particle size due to agglomeration. On the other hand, an increase in metal mixing decreases the surface area and pore volume, as can be seen from Table 1. The decrease in the total surface area can be attributed to the agglomeration of NiO particles on the Fe₂O₃ support, which is in line with the particle size calculated using XRD.

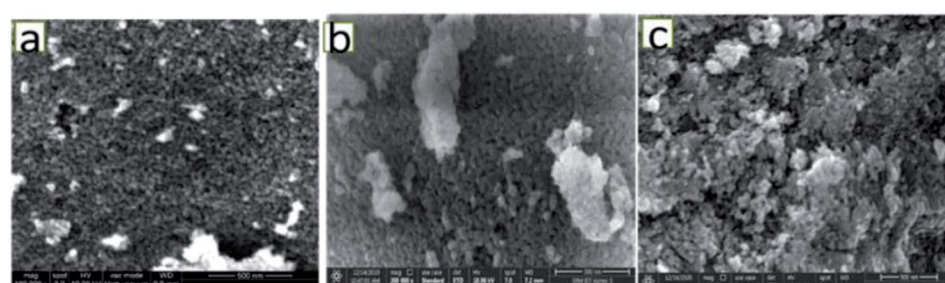
3.2. Plasma energy deposition into the packed bed reactor

Fig. 4 shows the effect of applied voltage on the specific input energy (SIE) delivered into the reactor packed with a 10NF catalyst, wherein it can be seen that the increase in applied voltage exponentially increases the SIE. It is worth mentioning that no significant difference in SIE was observed for the different catalyst packed reactors. The increase in applied voltage increases the charge build-up across the dielectric material and thus increase the power injected into the system. Therefore, it can be proposed that the enhanced charge improves the CO₂ conversion under similar operating

Table 1 Physicochemical properties of the various catalysts

Catalyst	Particle size (nm)		Metal mixing ^b (%)	S_{BET}^c (m ² g ⁻¹)	Pore volume (cm ³ g ⁻¹)	Pore size (Å)
	NiO	Fe ₂ O ₃				
Fe ₂ O ₃	—	32	—	NA	NA	NA
NiO	11	—	—	NA	NA	NA
5NF	40.8	20.4	5.2	23.5	0.15	195.6
10NF	178	29.9	10.3	9.1	0.03	28.5
15NF	8934	25.7 ^a	18.7	3.6	0.07	13.8

^a The ICCD database reference no 00-039-1346 peak at the highest intensity at 35.631 was used. ^b Results based on EDX analysis. ^c The specific surface area obtained from BET measurements.

Fig. 3 FESEM images of (a) 5% NiO–Fe₂O₃, (b) 10% NiO–Fe₂O₃, and (c) 15% NiO–Fe₂O₃.

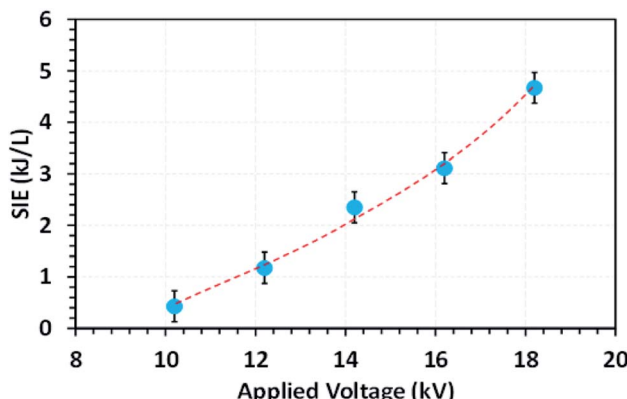


Fig. 4 The evolution of the SIE as a function of the applied voltage (feed flow rate: 100 mL min^{-1} , $\text{CO}_2/\text{H}_2 = 1:3$, frequency: 50 Hz).

conditions. The detailed plasma diagnostics were evaluated and the results are shown in Fig. S4 in the ESI.†

3.3. Thermal catalysis study

The catalyst bed temperature was linearly varied from 30 to 250 °C and the CO_2 conversion at different temperatures is shown in Fig. 5. We observed that for all of the catalysts the CO_2 conversion increases with an increase in temperature. Moreover, even at 250 °C the pure metal oxides *i.e.* NiO and Fe_2O_3 exhibited around 3.5% and <1% CO_2 conversion, respectively (results not reported in the figure). On the one hand, at 200 °C the CO_2 conversion increased from 1.7 to 3.7% upon increasing the NiO mixing from 5 to 15%. On the other hand, at 250 °C the mixing of 5% NiO with Fe_2O_3 improved the CO_2 conversion by three-fold (11.7%) under similar operating conditions. However, a further increase in the amount of NiO mixing exhibited a negative effect, *i.e.*, decreased the CO_2 conversion to 9% (10% NiO) and 7.5% (15% NiO). This decrease in conversion with an increase in NiO mixing could be attributed to the (i) NiO particle size and (ii) the oxidation of products such as CH_4 and CH_3OH to CO_2 at high temperatures. As reported in Table 1, the NiO particle size increased significantly with an increase in the

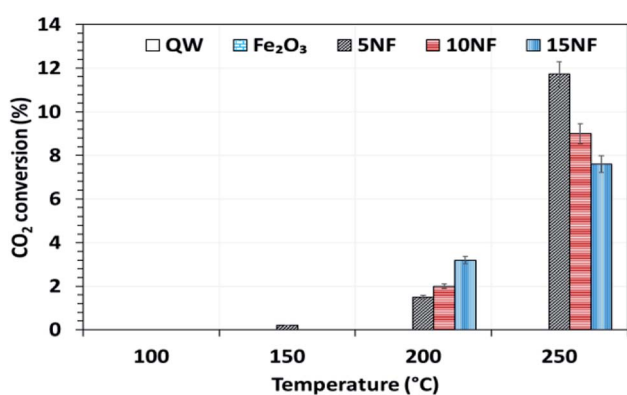


Fig. 5 The influence of temperature on CO_2 conversion for the different catalysts. Reaction conditions: catalyst, 0.5 g; $\text{H}_2/\text{CO}_2 = 75/25$, 100 mL min^{-1} ; $P = 1 \text{ atm}$.

amount of NiO mixing. The bigger the NiO particle size the more difficult it is to reduce compared to small sized NiO particles, as hydrogen mass transfer is hindered.³⁴



Fig. 6 shows the CH_3OH yield as a function of temperature varied between 100 and 250 °C. It can be observed that the CH_3OH yield increases with an increase in temperature. At 200 °C, the increase in NiO mixing from 5% to 10% increases the CH_3OH yield from 0.4 to 1%, respectively. At 250 °C, a maximum yield of 3.2% of CH_3OH was obtained for the 10NF catalyst. However, a further increase in the amount of NiO to 15% exhibited no CH_3OH formation. From the XRD results, it can be observed that the increase in NiO mixing (15NF) leads to the formation of NiFe_2O_4 and large particle size. Thus, it is suggested that spinel structures and larger NiO particles do not favour CH_3OH formation in thermal catalysis. This could be due to weaker and/or no chemisorption of CO and H_2 on spinels, as evidenced by Zhang *et al.*³⁹ The authors synthesised $\text{Ni}/\alpha\text{-Al}_2\text{O}$ for CO_2 hydrogenation to CH_4 . It was evident that nickel aluminate spinel structures (NiAl_2O_4) were formed on the catalyst surface, which was confirmed by XRD. NiAl_2O_4 is inactive towards the chemisorption of H_2 and CO and thus CH_4 is the main product quantified. Thus, it is thought that the species required for CH_3OH does not bind to the 15NF catalyst surface. Indeed, during CH_3OH synthesis the binding energy of intermediates (namely CO , formate others) is of prime importance as it determines the nature of the product. As reported in Fig. S1 in the ESI,† the pyridine adsorption study revealed that an increase in the amount of NiO also increased the number of Lewis basic sites. Therefore, the CO_2 adsorption on the catalyst surface also increases and more CO_2 conversion is expected, however, it should also be noted that the nature of the product is dependent on the intermediate binding strength. If

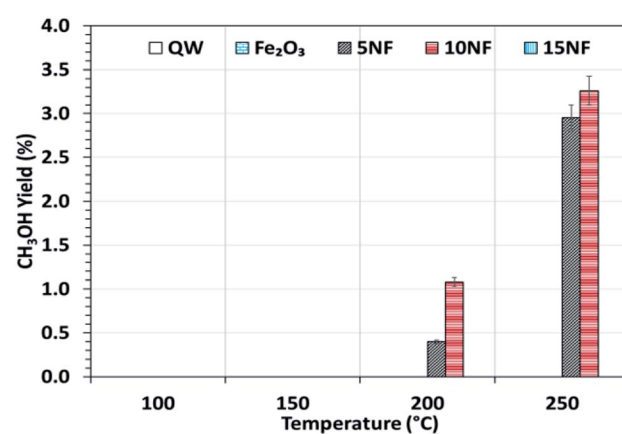


Fig. 6 CH_3OH yield as a function of the reaction temperature. Reaction conditions: catalyst, 0.5 g; $\text{H}_2/\text{CO}_2 = 75/25$, flow rate, 100 mL min^{-1} ; $P = 1 \text{ atm}$.

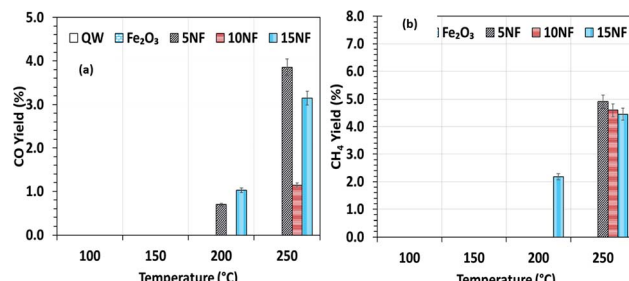


Fig. 7 (a) CO yield and (b) CH₄ yield as a function of the catalyst bed temperature.

intermediates (CO, formate) are strongly adsorbed on the NiO surface then this leads to CH₄ formation, *i.e.*, the Boudouard reaction is dominant, as reported in eqn (3) and (4).

By mixing metal oxides with different binding strengths toward the intermediates (CO and formate), a binary metal oxide mixture with optimum binding energy for the intermediates could be prepared. The optimum binding energy means that the intermediates are neither adsorbed strongly nor loosely on the catalyst surface. On the one hand, as we stated above, if the intermediates (CO and formate), adsorb strongly on NiO this leads to CH₄ formation, on the other hand, if CO adsorbs weakly (for example on Fe₂O₃), it is easily desorbed into the gas phase. Indeed, both sets of conditions significantly decrease the CH₃OH production. Thus, it is proposed that 10NF shows the optimum binding energy with the intermediates and thus the highest yield of CH₃OH.

To investigate the role that the amount of NiO has on CO and CH₄ formation, the respective yields were calculated as a function of temperature and the results are reported in Fig. 7(a) and (b). We observed that at 200 °C, the CO yield increased from 0.7% to 1.2% upon increasing the NiO content from 5% to 15%. Notably, with the 10NF catalyst, CO was not quantified at the reactor downstream. This result supports our hypothesis that all of the CO adsorbed with the optimum binding energy on the 10NF catalyst is converted to CH₃OH. Moreover, at 250 °C, the CO yield decreases with an increase in NiO mixing. It should also be noted that 10NF exhibits the lowest yield of CO, nevertheless, it exhibits the highest yield of CH₃OH (Fig. 6). These findings provide evidence for the fact that CO is converted into CH₃OH on the catalyst surface.

As can be seen in Fig. 7(b), only 15NF exhibits around 2.1% CH₄ yield at 200 °C. Moreover, it is noted that with an increase in the reaction temperature the CH₄ yield also increases.

Remarkably, at 250 °C, the CH₄ yield decreases with an increase in the amount of NiO. This CH₄ formation can be correlated to a high-temperature Boudouard reaction, *i.e.*, hydrogenation of carbon (C) to CH₄. Furthermore, the decrease in the CH₄ yield can be attributed to the oxidation of CH₄ to CO₂, thus decreasing the net CO₂ conversion.

3.4. Effect of plasma discharge on the CO₂ conversion and CH₃OH yield

It should be noted that at room temperature the plasma discharge does not show any CO₂ conversion. On the one hand,

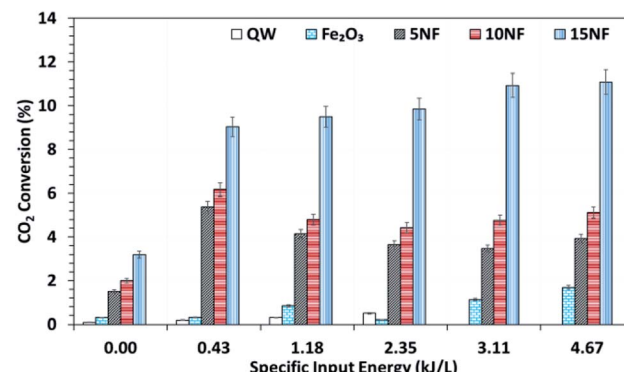


Fig. 8 CO₂ conversion at 200 °C as a function of the SIE. The SIE was varied between 0.43 and 4.67 kJ L⁻¹ via changing the applied voltage at a fixed frequency of 50 Hz.

up to 150 °C, the plasma-thermal catalytic process exhibits less than 1% CO₂ conversion. On the other hand, at 250 °C, despite around 10% CO₂ conversion, CH₄ was the major product in the thermal catalytic process. Moreover, we also found that when plasma discharge was ignited above 14 kV (2.6 kJ L⁻¹) at 250 °C, owing to the exothermic reaction and plasma injected power, the quartz reactor was broken (repeated five times with a similar result observed). Therefore, the effect of plasma discharge on CO₂ conversion and product distribution was investigated only at 200 °C and the results are reported in Fig. 8 and 9 as a function of specific input energy (SIE).

As showed in Fig. 8, without plasma discharge (denoted by 0.00 kJ L⁻¹), the CO₂ conversions were 1.5%, 2%, and 3.2% for 5NF, 10NF and 15NF, respectively. Interestingly, when plasma discharge was added (SIE of 0.43 kJ L⁻¹, 0.8 W, 10.2 kV) the conversions increased to 5.4%, 6.2%, 10.2% for 5NF, 10NF and 15NF, respectively. Indeed, the three-fold increase in CO₂ conversion could be due to the synergism between the plasma discharge and the catalyst.³⁰ The plasma discharge along with thermal catalysis leads to changes in discharge behaviour and the plasma parameters can be found in Fig. S4–S8 in the ESI.† The inductive effect of heating and applying plasma is crucial to

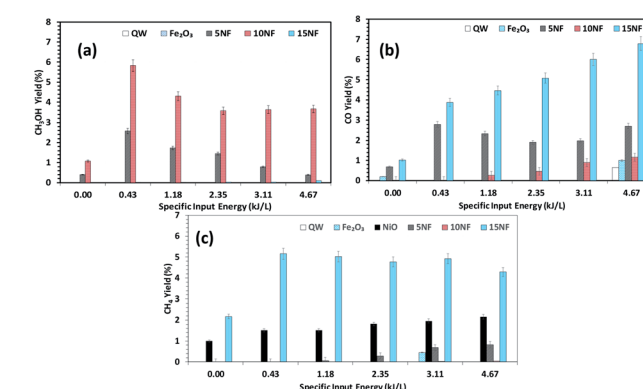


Fig. 9 Effects of the SIE on the product distribution at 200 °C. The yield of (a) CH₃OH, (b) CO, and (c) CH₄. Experimental conditions: catalyst, 0.5 g; H₂ : CO₂, 3 : 1; total flow rate, 100 mL min⁻¹.



increasing the effective capacitance by virtue of charge separation. Remarkably, the CO_2 conversion decreases upon an increase in the SIE. For example, when SIE was increased from 0.43 to 4.67 kJ L^{-1} the CO_2 conversion decreased from 5.4% to 3.9% and 6.2% to 5.1% for the 5NF and 10NF catalysts, respectively. However, for the 15NF catalyst, the CO_2 conversion increased from 9% to 11% with increasing SIE. The decrease in CO_2 conversion for the 5NF and 10NF catalysts can be attributed to the water gas shift reaction (WGSR), as reported in eqn (5). The Ni-based catalyst is very active towards the WGSR, and the CO molecules are converted into CO_2 .^{18,40}



Fig. 9(a)–(c) shows a comparison of the yields of the major products quantified at the reactor downstream as a function of SIE at 200 °C. We evidenced that, similar to CO_2 conversion, the CH_3OH yield also increased when the plasma discharge was ignited. This finding emphasises the fact that plasma discharge activates the catalyst surface at low temperatures and facilitates the liquid fuel CH_3OH production. As can be seen in Fig. 9(a), around 6% CH_3OH yield is achieved with the 10NF catalyst at 0.43 kJ L^{-1} SIE, which is six-fold higher than the yield obtained under similar operating conditions in the absence of plasma. However, an increase in SIE had a negative effect on the CH_3OH yield for both the 5NF and 10NF catalysts. The CH_3OH yield decreases with increasing SIE, and around 4% is obtained with 4.67 kJ L^{-1} SIE. The decrease in the CH_3OH yield can be attributed to (i) the decrease in CO_2 conversion as demonstrated in Fig. 8 and (ii) the decomposition of the produced CH_3OH to CO_2 . Notably, similar to the thermal catalytic process (Fig. 6) CH_3OH was not produced with the 15NF catalyst for all of the investigated SIE values. This can be ascribed to the weak/absence of chemisorption of CO and H_2 to produce CH_3OH .

As reported in Fig. 9(b), at 200 °C the plasma discharge significantly improves the CO yield for all of the studied catalysts. Indeed, with the 15NF catalyst, the CO yield increased with increasing SIE. The enhanced CO yield can be attributed to the improved CO_2 conversion, as shown in Fig. 8. Thus, it can be proposed that the inverse spinel NiFe_2O_4 assists the CO_2 splitting into CO rather than undergoing a hydrogenation reaction to form CH_3OH . Remarkably, the 10NF catalyst exhibited a maximum of 1% CO yield at 4.67 kJ L^{-1} , since a maximum of converted CO_2 was hydrogenated to CH_3OH , as shown in Fig. 9(a). As can be seen in Fig. 2, the PXRD pattern confirms that the 15NF catalyst has an inverse spinel NiFe_2O_4 structure (ICDD database reference number 01-086-2267). In NiFe_2O_4 , the active metal is encapsulated in the lattice of Fe_2O_3 making it difficult to reduce NiO to Ni at low temperature.⁴¹ Moreover, the NiO particles that are not encapsulated in the crystal lattice assist the conversion of CO_2 to CO and hydrogenation products such as CH_4 . In our previous study, we confirmed that the pure NiO catalyst selectively produces CH_4 and CO.³¹

As shown in Fig. 9(c), only the 15NF catalyst produces a significant amount of CH_4 . We also showed that the coupling of plasma at 200 °C doubled the CH_4 yield. Moreover, the

increase in SIE does not significantly influence the CH_4 yield. Thus, it can be proposed that when the NiO mixing reaches an optimum value only then it does facilitate the further conversion of formate (which is one of the intermediates in CO_2 to CH_4 conversion) into CH_4 .³⁵ Therefore, the catalyst becomes more selective towards CH_4 rather than other products such as CO and CH_3OH . Moreover, the CH_4 production and the reverse WGSR are competitive reactions and an increase in applied voltage facilitates CO formation, as shown in Fig. 9(b).

These findings enabled us to propose the following hypotheses: (i) at 200 °C, the plasma discharge on the catalyst significantly modifies the catalyst surface, thus the catalytic activity decreases in line with the plasma treatment time and (ii) the NiO particle size is modified by the plasma discharge. To provide evidence to prove these hypotheses, the catalysts before and after plasma treatment were characterized using PXRD, TEM and XPS techniques, with the results discussed in the following section.

4. Effects of plasma discharge on catalyst changes

Fig. 10 shows a comparison of the PXRD patterns of the catalyst before and after 30 min of plasma treatment at 200 °C with 2.4 kJ L^{-1} SIE at a 1 : 3 feed ratio of $\text{CO}_2 : \text{H}_2$ (100 mL min^{-1}). After plasma treatment, the 5NF and 10NF catalysts show different PXRD patterns compared to their patterns recorded as fresh catalysts. Thus, it can be concluded that the plasma discharge at low temperature brings about significant changes to the catalyst surface. We observed two important changes in the PXRD patterns: (i) the oxidation state of Fe is reduced from +3 to a mixture of +1 and +2, *i.e.* Fe_2O_3 to Fe_3O_4 and (ii) the NiO particle size is significantly reduced. Indeed, in thermal catalysis, even under reducing conditions at 200 °C, the catalyst does not show any significant changes. However, the additional energy provided by plasma discharge lowers the activation energy barrier and thus results in changes. Remarkably, in terms of the 15NF catalyst after plasma treatment, no significant modification was observed in the PXRD pattern. Moreover, the PXRD pattern of the synthesised 15NF catalyst matches an inverse spinel NiFe_2O_4 reference pattern from the ICDD database (reference number 01-086-2267). The NiFe_2O_4 is magnetic and

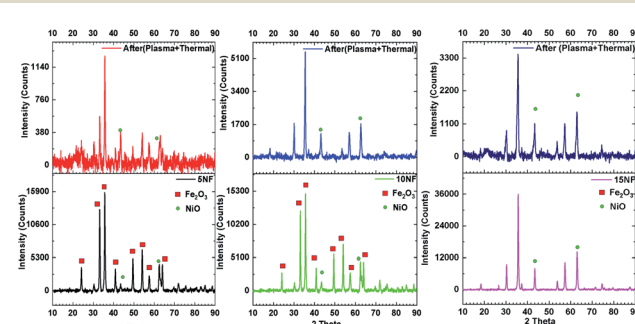


Fig. 10 PXRD patterns of the catalyst before (bottom) and after (top) plasma treatment at 200 °C.



Table 2 Effects of plasma discharge on the NiO particles

Catalyst	NiO particle size (nm)		d-spacing (Å)		Lattice parameter (Å)	
	Before	After	Before	After	Before	After
5NF	40.8	13.2	3.25	3.25	6.51	6.51
10NF	178	17.6	3.14	1.97	6.28	3.95
15NF	8934	13.1	4.62	2.42	9.25	4.85

crystallises in a face centred cubic structure. The NiFe_2O_4 has an inverse spinel structure, wherein Ni^{2+} occupies octahedral sites and Fe^{3+} occupies half of the tetrahedral and octahedral voids. The active metal oxide NiO is encapsulated in the lattice of Fe_2O_3 and it is difficult to reduce NiO under our operating conditions.³⁸ After plasma treatment, the 10NF catalyst PXRD pattern exactly matches that of NiFe_2O_4 , similar to the 15NF catalyst. However, the 10NF catalyst exhibits a higher CH_3OH yield than 15NF.

The only difference between these two catalysts is the plasma discharge assisted inverse spinel formation, at low temperature, from the $\text{NiO-Fe}_2\text{O}_3$ mixture. Thus, the enhanced catalytic activity of 10NF can be attributed to its particle size, the nature of its surface and the mixture of the formation of inverse spinel NiFe_2O_4 and Fe_3O_4 .

Table 2 shows a comparison of the impact that plasma discharge has on the particle size and lattice parameters of NiO calculated from the PXRD patterns. This is evidence that the plasma discharge on the catalyst surface significantly reduces the particle size of NiO, irrespective of the amount of mixing. The d-spacing and lattice parameters of the 10NF and 15NF catalysts were also modified by plasma discharge, as observed in the shifting of the diffraction peaks to lower 2θ values. The shifting of the peaks is a result of a reduction in the NiO particle size. Moreover, the plasma discharge does not affect the Fe_2O_3 particle size. It should also be noted that after 30 min of plasma treatment the 15NF catalyst exhibited a particle size of around 13 nm, however, CH_3OH was not produced, as shown in Fig. 9(a). Thus, it can be concluded that rather than the particle size, the nature of the spinel structure significantly influences the CO_2 conversion and CH_3OH selectivity.

To provide evidence for the reduction in the particle size by plasma treatment, the plasma-treated 10NF catalyst was characterized by high-resolution TEM (HRTEM) and the results are shown in Fig. 11. The images reveal that the NiO particles are spherical in structure, the average particle size is 15.1 nm and the average d-spacing value is 0.228 nm (2.28 Å).

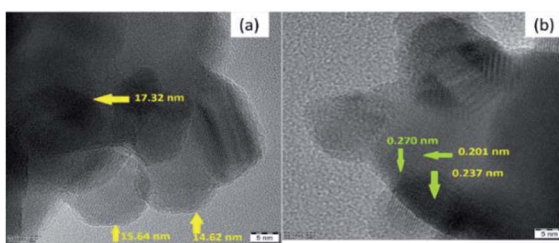


Fig. 11 HRTEM images of the plasma-treated 10NF catalyst.

As shown in Table 2, after plasma treatment, from PXRD the calculated NiO particle size for 10NF was found to be 17.6 nm and the d-spacing was 0.197 nm (1.97 Å). The observed TEM and calculated PXRD result are in good agreement. Thus, it can be concluded that the plasma discharge at 200 °C on the powder sample significantly reduces the particle size and improves the CO_2 conversion and CH_3OH selectivity.

XPS analysis was carried out to obtain further information on the elemental composition and oxidation state of 10% $\text{NiO-Fe}_2\text{O}_3$ (10NF) catalyst before and after plasma treatment, with the results reported in Fig. 12(a)–(f). The X-ray source of the XPS measurements was Mg $\text{K}\alpha$, and the binding energies of the Fe 2p and Ni 2p spectra were calibrated according to the binding energy of C 1s of the adventitious C at 284.5 eV. The survey spectrum, before and after plasma treatment, exhibited only Fe, Ni and O along with C peaks, moreover, no significant difference was observed. As can be seen from Fig. 12(a), before plasma treatment two distinct peaks centered at 710.58 and 724.02 eV corresponding to the $\text{Fe 2p}_{3/2}$ and $\text{Fe 2p}_{1/2}$ spin-orbit peaks, respectively, were observed, identifying the Fe^{3+} oxidation state on the $\text{NiO-Fe}_2\text{O}_3$ surface.⁴² Interestingly, after plasma exposure for 30 min, the peak at 710.58 eV deconvolutes into two peaks centred at 710.08 and 711.78 eV. The oxidation states affect the binding energy of the material. The peak at 710.08 eV can be attributed to Fe^{2+} and the peak at 711.78 eV can be ascribed to Fe^{3+} . These findings emphasise that plasma treatment reduces Fe^{3+} partially to Fe^{2+} .^{39,43} Moreover, it should be noted that before plasma treatment there are fewer intensity signals for the shakeup satellites at 732.23 and 718.44 eV. Furthermore, after plasma treatment the intensity slightly increased and the peaks moved to higher binding energies (719.2 and 732.8 eV) indicating the presence of a separate hematite phase in the sample.

The Ni 2p spectra, before and after plasma treatment, are compared in Fig. 12(c) and (d). Before plasma treatment the sample exhibits two spin-orbit peaks of $\text{Ni 2p}_{1/2}$ and $\text{Ni 2p}_{3/2}$ at

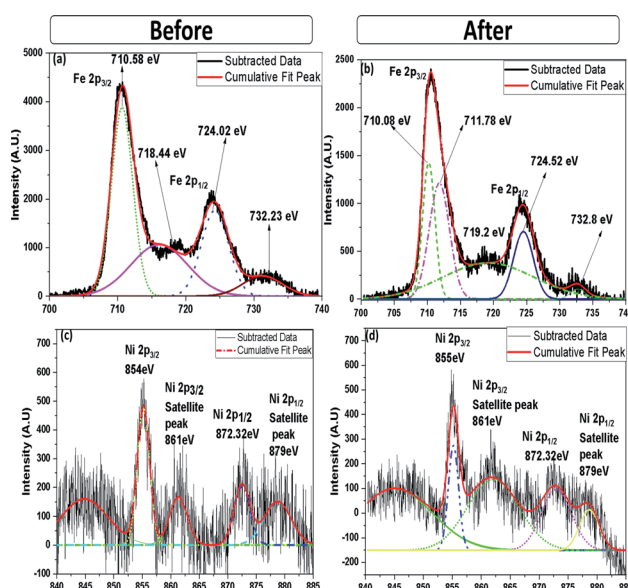


Fig. 12 High-resolution (a) Fe 2p and (c) Ni 2p XPS spectra (before plasma treatment) and (b) Fe 2p and (d) Ni 2p XPS spectra (after plasma treatment).



872.32 and 854 eV, with two shakeup satellite peaks at 879 and 861 eV, indicating that Ni^{2+} and Ni^{3+} co-existed in the $\text{NiO-NiFe}_2\text{O}_4$ sample.⁴⁴ Similar peaks also appeared for the plasma-treated sample, however, the intensity of the peaks at 861 and 879 eV decreased. Therefore, it can be suggested that the plasma treatment under a reducing atmosphere modifies the Ni^{2+} to Ni^{3+} ratio. Moreover, it should be noted that the appearance of the double peak features in the Ni 2p spectrum along with their consecutive shake-up satellite peaks reveal the magnetic chemical states Ni^{2+} and Ni^{3+} on the plasma-treated catalyst surface.⁴⁵

From the extensive catalyst characterisation, before and after plasma treatment, it is proposed that the mixture of compounds such as $\text{NiO-Fe}_2\text{O}_3$, inverse spinel NiFe_2O_4 and Fe_3O_4 assist CO_2 conversion and CH_3OH production. Moreover, the inverse spinel NiFe_2O_4 , *i.e.* 15% $\text{NiO-Fe}_2\text{O}_3$ catalyst, shows CO_2 conversion, however, it assists only CH_4 production. Nevertheless, *in situ* surface investigation is needed to confirm the role of the various phases of Fe_2O_3 in the conversion of CO_2 under plasma discharge.

5. Conclusions

In the present work, it was demonstrated that CH_3OH could be synthesised using the binary metal oxide $\text{NiO-Fe}_2\text{O}_3$. The pure metal oxides, namely NiO and Fe_2O_3 , exhibit no significant amount of CO_2 conversion. However, for the binary mixed oxide, CO_2 conversion and CH_3OH production were greatly increased. We also provided evidence that the intermediate CO is adsorbed on the catalyst surface with modest energy, thus it can be easily hydrogenated to CH_3OH . With an increase in the amount of NiO in Fe_2O_3 , the particle size increased tremendously and decreased the CO_2 conversion during thermal catalysis.

A synergistic effect is observed when plasma is combined with thermal heating, and this improves CO_2 conversion. The CO_2 conversion and CH_3OH yield were increased by 3- and 5-fold, respectively, at a SIE of 0.43 kJ L^{-1} over the 10NF catalyst. The observed synergism is due to the generation of reactive species on the catalyst surface *via* plasma discharge, which speeds up CO_2 conversion and CH_3OH formation. The 10NF catalyst exhibited the best CH_3OH production, whereas the 15NF catalyst was selective towards CH_4 . It can be proposed that a low amount of NiO mixing (<10%) leads to the RWGS reaction, yielding CO as the main product, however, a high amount of NiO mixing leads to CH_4 formation.

We also showed that plasma treatment at 200 °C significantly reduced the NiO particle size, however, it did not affect the Fe_2O_3 particles. Moreover, it was demonstrated that the plasma treatment induced phase transformation at low temperatures and led to the formation of a mixture spinel structure. The catalyst with a mixed spinel structure assisted CO_2 conversion and CH_3OH production.

Conflicts of interest

There are no conflicts to declare.

Acknowledgements

The authors greatly acknowledge the Science & Engineering Research Board, Department of Science & Technology, Government of India (SERB, File No. ECR/2016/001457) for financial support. We acknowledge the Nanotechnology Research Centre (NRC), and the HRTEM and HRSEM facility at SRMIST for providing research facilities.

References

- 1 G. P. Peters, G. Marland, C. Le Quere, T. Boden, J. G. Canadell and M. R. Raupach, *Nat. Clim. Change*, 2011, **2**, 2–4.
- 2 J. D. Shakun, P. U. Clark, F. He, S. A. Marcott, A. C. Mix and Z. Y. Liu, *Nature*, 2012, **484**, 49–55.
- 3 N. P. Gillett, V. K. Arora, K. Zickfeld, S. J. Marshall and W. J. Merryfield, *Nat. Geosci.*, 2011, **4**, 83–87.
- 4 M. E. Boot-Handford, J. C. Abanades, E. J. Anthony, M. J. Blunt, S. Brandani and N. Mac Dowell, *Energy Environ. Sci.*, 2014, **7**, 130–189.
- 5 M. L. Szulczewski, C. W. MacMinn, H. J. Herzog and R. Juanes, *Proc. Natl. Acad. Sci. U. S. A.*, 2012, **109**, 5185–5189.
- 6 C. Das Neves Gomes, O. Jacquet, C. Villiers, P. Thuery, M. Ephritikhine and T. Cantat, *Angew. Chem.*, 2012, **51**, 187–190.
- 7 A. Taheri Najafabadi, *Int. J. Energy Res.*, 2013, **37**, 485–499.
- 8 M. Burkhardt and G. Busch, *Appl. Energy*, 2013, **111**, 74–79.
- 9 F. Studt, I. Sharafutdinov, F. Abild-Pedersen, C. F. Elkjaer, J. S. Hummelshøj and S. Dahl, *Nat. Chem.*, 2014, **6**, 320–324.
- 10 M. Taherimehr and P. P. Pescarmona, *J. Appl. Polym. Sci.*, 2014, **131**, 41141–41157.
- 11 W. Wang, S. P. Wang, X. B. Ma and J. L. Gong, *Chem. Soc. Rev.*, 2011, **40**, 3703–3727.
- 12 X. B. Lu and D. J. Daresbourg, *Chem. Soc. Rev.*, 2012, **41**, 1462–1484.
- 13 M. Bowker, *ChemCatChem*, 2019, **11**, 4238–4246.
- 14 X. Tu, H. J. Gallon, M. V. Twigg, P. A. Gorry and J. C. Whitehead, *J. Phys. D: Appl. Phys.*, 2011, **44**, 274007.
- 15 J. Ren, X. Qin, J.-Z. Yang, Z.-F. Qin, H.-L. Guo, J.-Y. Lin and Z. Li, *Fuel Process. Technol.*, 2015, **137**, 204–211.
- 16 J. Wei, Q. Ge, R. Yao, Z. Wen, C. Fang, L. Guo, H. Xu and J. Sun, *Nat. Commun.*, 2017, **8**, 15174.
- 17 C. Zhou, J. Shi, W. Zhou, K. Cheng, Q. Zhang, J. Kang and Y. Wang, *ACS Catal.*, 2020, **10**, 302–310.
- 18 X. Jiang, X. Nie, X. Guo, C. Song and J. G. Chen, *Chem. Rev.*, 2020, **120**, 7984–8034.
- 19 W. Li, H. Wang, X. Jiang, J. Zhu, Z. Liu, X. Guo and C. Song, *RSC Adv.*, 2018, **8**, 7651–7669.
- 20 D. Wierzbicki, M. V. Moreno, S. Ognier, M. Motak, T. Grzybek, P. Da Costa and M. E. Gálvez, *Int. J. Hydrogen Energy*, 2020, **45**, 10423–10432.
- 21 X. Ma, S. Li, M. Ronda-Lloret, R. Chaudhary, L. Lin, G. van Rooij and V. Hessel, *Plasma Chem. Plasma Process.*, 2019, **39**, 109–124.
- 22 E. Jwa, S. B. Lee, H. W. Lee and Y. S. Mok, *Fuel Process. Technol.*, 2013, **108**, 89–93.

23 I. Michielsen, Y. Uytdenhouwen, J. Pype, B. Michielsen, J. Mertens, F. Reniers, V. Meynen and A. Bogaerts, *Chem. Eng. J.*, 2017, **326**, 477–488.

24 L. Wang, Y. Yi, H. Guo and X. Tu, *ACS Catal.*, 2017, **8**, 90–100.

25 L. Sivachandiran, P. Da Costa and A. Khacef, *Appl. Surf. Sci.*, 2020, **501**, 144175.

26 I. Belov, S. Paulussen and A. Bogaerts, *Plasma Sources Sci. Technol.*, 2016, **25**, 015023.

27 K. Van Laer and A. Bogaerts, *Energy Technol.*, 2015, **3**, 1038–1044.

28 J. Sentek, K. Krawczyk, M. Młotek, M. Kalczewska, T. Kroker, T. Kolb, A. Schenk, K.-H. Gericke and K. Schmidt-Szałowski, *Appl. Catal., B*, 2010, **94**, 19–26.

29 H. K. Song, J.-W. Choi, S. H. Yue, H. Lee and B.-K. Na, *Catal. Today*, 2004, **89**, 27–33.

30 M. Kraus, W. Egli, K. Haffner, B. Eliasson, U. Kogelschatz and A. Wokaun, *Phys. Chem. Chem. Phys.*, 2002, **4**, 668–675.

31 A. Bill, B. Eliasson, U. Kogelschatz and L. M. Zhou, *Stud. Surf. Sci. Catal.*, 1998, **114**, 541–544.

32 B. Eliasson, U. Kogelschatz, B. Xue and Li-M. Zhou, *Ind. Eng. Chem. Res.*, 1998, **37**, 3350–3357.

33 M. Ronda-Lloret, Y. Wang, P. Oulego, G. Rothenberg, X. Tu and N. R. Shiju, *ACS Sustainable Chem. Eng.*, 2020, **8**, 17397–17407.

34 N. Joshi and S. Loganathan, *Plasma Process Polym.*, 2021, **18**(5), 2000104.

35 T. C. Manley, *Trans. Electrochem. Soc.*, 1943, **84**, 83–96.

36 T. Butterworth, R. Elder and R. Allen, *Chem. Eng. J.*, 2016, **293**, 55–67.

37 K. Zhao, W. Wang and Z. Li, *J. CO₂ Util.*, 2016, **16**, 236–244.

38 Z. Zhang, Y. Tian, L. Zhang, S. Hu, J. Xiang, Y. Wang and X. Hu, *Int. J. Hydrogen Energy*, 2019, **44**, 9291–9306.

39 Y. Zhang, W. Chu, W. Cao, C. Luo and X. Wen, A Plasma-Activated Ni/α-Al₂O₃ Catalyst for the Conversion of CH₄ to Syngas, *Plasma Chem. Plasma Process.*, 2000, **20**, 137–144.

40 C. Ratnasamy and J. P. Wagner, *Catal. Rev.*, 2009, **51**, 325–440.

41 R. Benrabaa, H. Boukhloouf, A. Löfberg, A. Rubbens, R. N. Vannier, E. Bordes-Richard and A. Barama, *J. Nat. Gas Chem.*, 2012, **21**, 595–604.

42 P. Li, E. Y. Jiang and H. L. Bai, *J. Phys. D: Appl. Phys.*, 2011, **44**, 075003.

43 K. D. Wright and A. R. Barron, *J. Carbon Res.*, 2017, **3**, 17.

44 G. Liu, X. Gao, K. Wang, D. He and J. Li, *Int. J. Hydrogen Energy*, 2016, **41**, 17976–17986.

45 J. S. Shaikh, R. C. Pawar, R. S. Devan, Y. R. Ma, P. P. Salvi, S. S. Kolekar and P. S. Patil, *Electrochim. Acta*, 2011, **56**, 2127.

